Full length article

Creep behavior of a precipitation-strengthened A2-B2 refractory high entropy alloy

Liu Yang [a], Sandipan Sen [a],[*], Daniel Schliephake [a], R. J. Vikram [a], Stephan Laube [a], Aparajita Pramanik [b], Ankur Chauhan [b], Steffen Neumeier [c], Martin Heilmaier [a], Alexander Kauffmann [a],[*]

[a] Institute for Applied Materials (IAM-WK), Karlsruhe Institute of Technology (KIT), Engelbert-Arnold-Str. 4, 76131 Karlsruhe, Germany
[b] Extreme Environments Materials Group, Department of Materials Engineering, Indian Institute of Science, Bengaluru, Karnataka 560012, India
[c] Friedrich-Alexander-Universität Erlangen-Nürnberg, Department of Materials Science & Engineering, Institute I: General Materials Properties, Martensstraße 5, 91058 Erlangen, Germany

ARTICLE INFO

ABSTRACT

Refractory compositionally complex alloys consisting of a disordered A2 matrix and ordered B2 precipitates mimic the microstructures of state-of-the-art, Ni-based superalloys with A1 matrix and $L1_2$ precipitates. The former are promising candidates for high-temperature applications because of their high melting points. 27.3Ta-27.3Mo-27.3Ti-8Cr-10Al (in at. %, TMT-8Cr-10Al) is a relevant example where this A2-B2, two-phase microstructure is formed by a precipitation reaction and remains stable even at temperatures close to the precipitate solvus temperature (T_S). The present study systematically addresses the creep response of polycrystalline TMT-8Cr-10Al at temperatures of 1000 °C and above. Compared to polycrystalline, single-phase A2 and B2 high entropy alloys, a substantially higher compression creep resistance is observed for the two-phase alloy while minimum creep rates comparable to those of state-of-the-art single-crystalline A1-$L1_2$ CMSX-4 are found. This is specifically remarkable considering the polycrystalline condition of TMT-8Cr-10Al, the open matrix A2 crystal structure and the close proximity of the test temperatures to the solvus temperature with 0.98 T_S compared to 0.85 T_S for CMSX-4. Consistent with a positive lattice misfit, directional coarsening of precipitates in TMT-8Cr-10Al is noted to be perpendicular to the compression direction after creep in grains with ⟨100⟩ close to the compression direction.

1. Introduction

The concept of high entropy alloys (HEAs) has attracted the attention of many researchers since its introduction in the early 2000s by Yeh et al. [1,2] and Cantor et al. [3]. While HEAs synthesized from 3d transition metals like Fe, Cr, Ni, Co and others have been of particular interest with respect to mechanical properties at ambient and low temperatures, the concept was soon extended to refractory high entropy alloys (RHEAs) by the seminal work of Senkov et al. [4–7]. RHEAs are composed of refractory elements and exhibit usually high melting points beyond 2000 °C leading to excellent compressive strength under quasi-static testing conditions even up to 1600 °C [5]. As all refractory elements suffer from catastrophic oxidation at intermediate and high temperatures [8], concepts to improve their oxidation resistance were developed and introduced by adding potentially passivating elements

like Al, Cr, etc. [9–12]. Particularly, RHEAs containing Ta, Cr and Ti were identified to provide a strategy to achieve oxidation resistance by the formation of a slowly growing rutile type oxide [8,12–15]. Even though this protective oxide does not contain Al, Al promotes its formation and is thus added as a required element in the alloys [14]. Furthermore, Al and Ti lead to a significant reduction of density [16–18] as compared to RHEAs composed of only refractory elements. When synthesized in close to equimolar composition and subjected to high-temperature homogenization treatments, many of the alloys from the Ta-Mo-Nb-Cr-Ti-Al system form single-phase material with disordered, body centered cubic (BCC) A2 (Strukturbericht designation) or ordered B2 crystal structure and low amounts of secondary phases [16–20].

Recently, considerable effort has been placed on advanced alloying strategies in non-equimolar, refractory compositionally complex alloys

* Corresponding authors.
E-mail addresses: sandipan.sen@kit.edu (S. Sen), alexander.kauffmann@kit.edu (A. Kauffmann).

(RCCAs) to mimic the microstructures of state-of-the-art, Ni-based superalloys with Strukturbericht A1 (face centered cubic, FCC) matrix and L1$_2$ precipitates. The analogous microstructure in RCCAs consists of a disordered A2 matrix and ordered B2 precipitates and the class of alloys is often referred to as refractory (or BCC) superalloys [21]. A huge variety of experimental [22–25] and theoretical considerations [26] were made to deliberately synthesize the A2-B2 microstructure. Particularly, within the Ta-Mo-Cr-Ti-Al system, alloys were identified that form the desired A2-B2 microstructures by a nucleation and growth process and the relevant reaction sequence of phase separation and ordering [27, 28].

In view of recent systematic creep studies by Gadelmeier et al. [29] and Liu et al. [30], this type of microstructural tailoring aimed at efficient precipitation strengthening seems imperative to achieve competitive creep performance over established high temperature materials. In these works, the single-phase A2, equimolar TiZrHfNbTa was investigated with respect to its tensile creep behavior at 980 °C (50 – 120 MPa) and 1100 °C (10 – 30 MPa) [29,30]. The minimum creep rates at both temperatures was higher than 10^{-7} s^{-1} and thus creep resistance is notably lower than that of a state-of-the-art, precipitation-strengthened, single-crystalline Ni-based superalloy (e.g., CMSX-4 with a L1$_2$ solvus temperature of approximately 1280 °C [31]). This discrepancy is not only attributed to the polycrystalline microstructure of TiZrHfNbTa, but also to the presence of a single-phase microstructure with solid solution strengthening only (absence of precipitation strengthening) as well as the commonly accepted faster diffusion in the non-closed packed A2 crystal structure. Furthermore, the microstructure was found to undergo a decomposition into A2 and A3 during creep [29].

Apart from the fundamental consideration of precipitation strengthening of an A2 matrix alloy by B2 precipitates, the detailed analysis of the microstructures after creep of the benchmark A1-L1$_2$ Ni-based superalloys has revealed significant microstructural changes induced by the creep deformation, the most prominent of which is rafting [32]. Rafting is a phenomenon of directional coarsening of the precipitates during creep deformation. A rafted microstructure is essential to maintain high creep resistance at high-temperature and low stress condition, which can increase the dislocation climb distance at the interface between L1$_2$ and A1 [33]. The lattice misfit between precipitate and matrix not only plays an important role in the formation of the rafted microstructure, but also affects the directional relationship between the rafted microstructure and the external stresses [34]. This means that the sign of the lattice misfit between matrix and precipitates, combined with the loading direction, influences the rafting behavior, with positive misfit leading to raft formation perpendicular to the compressive loading direction (N-type) but parallel to loading direction in tension (P-type) [35]. The lattice misfit (in analogy to the Ni-based superalloy case) can be quantified by the following equation:

$$\delta = \frac{2(a_{B2} - a_{A2})}{a_{B2} + a_{A2}} \tag{1}$$

where, δ represents the lattice misfit, while a_{A2} and a_{B2} represent the lattice parameters of A2 and B2, respectively. It has to be noted that most of the studies focused on single crystalline (SX) superalloys and loading was applied with uniaxial stress along ⟨001⟩. Even in the studies involving polycrystals (PX), the N-type rafting was observed only for grains with close to ⟨001⟩ parallel to the loading direction [36]. A schematic for this relationship between the sign of δ and the type of uniaxial loading as reported for Ni- and Co- based superalloys is shown in Fig. S1 of the Supplementary Material.

Despite the considerable efforts to develop A2-B2 RCCAs, there is currently no systematic assessment of the creep behavior and mechanisms of such alloys as well as the impact of creep deformation on the A2-B2 microstructure available in literature. Thus, we present a first systematic study on the creep behavior of 27.3Ta-27.3Mo-27.3Ti-8Cr-10Al (in at. %, abbreviated by TMT-8Cr-10Al in what follows) as a

model alloy introduced by Laube et al. [27,28]. It has been confirmed via differential scanning calorimetry (DSC) that B2 precipitates form by a diffusion-controlled precipitation below temperatures of around 1055 °C [27]. Additionally, a stable two-phase microstructure was found even after prolonged exposure at temperatures close to the solvus temperature [28]. These findings suggest promising prospect for achieving high-temperature creep resistance in this alloy.

In detail, we focus on the following fundamental research questions:

1. How does the creep behavior of a two-phase, precipitation-strengthened A2-B2 TMT-8Cr-10Al compare to that of state-of-the-art, single-crystalline Ni-based superalloys with A1-L1$_2$ microstructure as well as to polycrystalline, single-phase A2 or B2 RHEAs?
2. How does the microstructure of TMT-8Cr-10Al evolve during the creep loading?
3. How do the microstructural changes depend on the lattice misfit between the B2 precipitates and the A2 matrix?

2. Experiments and materials

TMT-8Cr-10Al was synthesized by repetitive arc melting under Ar atmosphere using an AM/0.5 furnace supplied by Edmund Bühler GmbH (Germany). The purities of the elements Ta, Mo, Ti, Cr, and Al provided by chemPUR GmbH (Germany), were 99.9 %, 99.95 %, 99.8 %, 99.99 %, and 99.99 %, respectively. One button, weighing approximately 150 g, was synthesized by five steps of flipping and re-melting. The button was then cast into a cuboid shape using a water-cooled Cu mold. Subsequently, the as-cast TMT-8Cr-10Al alloy was wrapped in Mo foil (to minimize oxidation) for homogenization at 1600 °C for 20 h to remove the as-cast dendritic microstructure. Heating and cooling rates of 100 K/h in a HTRT 70-600/18 resistance tube furnace (Carbolite Gero GmbH & Co. KG, Germany) were applied. The atmosphere was established by three evacuation cycles and backfilling with continuous Ar flow in order to prevent oxidation. Further details on the synthesis process can be found in previous studies [27,28].

To investigate the microstructure, samples cut from the button by electrical discharge machining (EDM) were first ground with SiC abrasive paper to P4000 grit. Afterwards, 3 μm and 1 μm polycrystalline diamond suspension were used for polishing for 5 min each. Then, the samples were polished for 10 min using a colloidal oxide polishing suspension provided by Buehler ITW (Germany) on a semi-automatic machine. The final preparation step was chemo-mechanical vibratory polishing using a non-crystallizing oxide polishing suspension provided by Struers (Germany) for at least 16 h. Scanning electron microscopy (SEM) was performed using a Zeiss LEO 1530 (Zeiss, Germany) at 20 kV acceleration voltage. Electron backscatter diffraction (SEM-EBSD) with an EDAX Digiview system (Ametek, USA) in a Zeiss Auriga 60 (Zeiss, Germany) was used to image the local crystallographic orientation and to identify secondary phases. Composition was determined by inductively coupled plasma-optical emission spectroscopy (ICP-OES) of the homogenized TMT-8Cr-10Al alloy and scanning electron microscopy-based energy dispersive X-ray spectroscopy (SEM-EDS) in the Zeiss Auriga 60 system with Octane Super-A detector (Ametek, USA). The levels of O and N impurities were detected in five samples of TMT-8Cr-10Al by carrier gas hot extraction (CGHE) utilizing a TC600 system supplied by Leco Instrumente GmbH, Germany. The density of the alloy was calculated according to Archimedes' principle by selecting five samples to calculate the average density. The density measurements were conducted with the balance ME204T/00 with a density measuring kit ME-DNY-43 from the company Mettler-Toledo GmbH (Germany).

For transmission electron microscopy (TEM), electron-transparent foils were prepared using a lift-out technique with a ThermoFisher Scios-2 (USA) system equipped with a dual beam focused ion beam (FIB). Initially, a protective platinum layer was deposited, followed by FIB sectioning at 30 kV with probe currents of 5 nA and 1 nA, respectively. The TEM lamellae were then lifted out and attached to a

molybdenum half-grid through platinum deposition. Subsequently, the lamellae were thinned to approximately 80 nm using various voltage and current combinations in the FIB. Final cleaning was performed at 2 kV and 10 pA for an extended period.

Diffraction contrast imaging was performed using a ThermoFisher Tecnai T20-ST (USA) TEM operated at 200 kV in parallel illumination mode. The atomic structure of the phases was investigated using scanning transmission electron microscopy (STEM) in a probe-corrected ThermoFisher Titan Themis (USA) TEM operated at 300 kV. The TEM foil was tilted to a low-index zone axis for diffraction contrast and atomic resolution imaging. Atomic resolution micrographs were acquired with a high-angle annular dark field (HAADF) detector and a camera length of 160 mm. Specimen drift during atomic resolution imaging was corrected using the drift-corrected frame integration (DCFI) function of the Velox software. Lattice parameters of the phases were estimated by filtering a specific spot in the fast Fourier transformation (FFT) of the high-resolution HAADF-STEM micrographs and measuring interplanar spacing with line profiles along multiple lattice planes in the Gatan Microscopy Suite software.

The samples for compression creep tests with dimensions of $(5 \times 3 \times 3)$ mm^3 were prepared by electrical discharge machining (EDM). Before creep testing, the surface of each sample was ground to remove the oxidation/EDM layer. Compression creep tests were carried out under vacuum $(5 \cdot 10^{-5}$ mbar), to exclude environmental effects on creep, utilizing a Z100 electro-mechanical universal testing machine provided by ZwickRoell GmbH & Co. KG (Germany) equipped with a vacuum furnace supplied by Maytec GmbH (Germany). The test temperatures ranged from 1000 °C to 1070 °C and true stresses of 50, 75, 100, 125, 150 and 175 MPa were applied. All compression creep tests were started after a duration of 30 min under a preload 50 N at the test temperature to ensure uniform temperature distribution. After the creep test, the samples were cooled to room temperature by furnace cooling and then prepared for microstructural investigations using the metallographic steps described above. At least three tests were performed at each test condition in order to ensure the relevance of the results. In order to track the impact of long-term heat treatment under the same conditions without external mechanical load, stress-free heat treatments were also performed at the same temperatures and durations compared to the compression creep tests. The samples used for heat treatment were wrapped in Ta foil and then sealed into fused silica tubes under Ar atmosphere to avoid oxidation during the heat treatment process. After quenching, microstructural studies were carried out on the heat-treated samples following the above-mentioned metallographic steps.

3. Results and discussion

3.1. Initial composition and microstructure

In order to assess the chemical composition of TMT-8Cr-10Al, ICP-OES and HCGE were conducted and the results are shown in Table 1. The composition of the constituent elements observed via ICP-OES is within the experimental accuracy range. The levels of O and N are found to be between 100 and 500 wt.-ppm and are comparable to other studies in RHEAs and RCCAs [27,37–39]. The chemical homogeneity of this alloy at the microscale determined by SEM-EDS was reported previously [27]. The experimental density of the alloy determined by the Archimedes method is 9.6 g cm^{-3}.
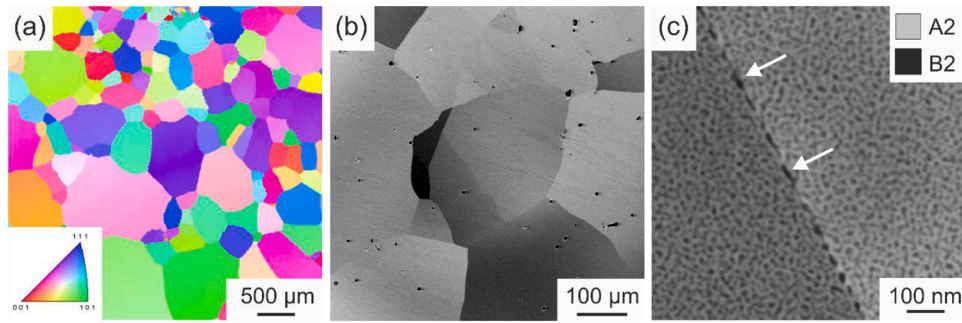
Fig. 1(a) shows an inverse pole figure (IPF) map of the TMT-8Cr-10Al obtained by SEM-EBSD in the as-homogenized condition. It can be observed that the orientation of the grains is random indicating no preferred orientation present in the initial microstructure. In the orientation-contrast SEM-BSE micrographs, a coarse-grained microstructure as well as some pores (displayed as dark features) are revealed, as shown in Fig. 1(b). The appearance of pores is due to the Kirkendall effect that occurs during homogenization of dendritic cast microstructures with significant Al enrichment in the interdendritic regions [40]. The mean grain size of the investigated samples is above 200 μm. At higher magnification, two different SEM-BSE contrasts within the grains at the nanoscale can be observed as shown in Fig. 1(c). Those contrasts are attributed to the difference in atomic number Z between A2 and B2. The composition of these phases was reported earlier [27], the continuous bright matrix is enriched in Ta and Mo while the dark precipitates are enriched in Al and Ti, with Cr distributed uniformly throughout the alloy. The bright matrix phase was identified as a disordered A2 and the discontinuous dark phase as ordered B2 precipitates via TEM experiments in Refs. [27,28]. Additional dark particles (marked with white arrows in (c)) of less than 0.1 vol. % were also observed at grain boundaries, which were previously identified to be Ti-rich nitrides resulting from N contamination during arc melting and homogenization [28]. However, the grain size of the material is considered coarse enough that grain boundary sliding does not significantly contribute to creep deformation in the present case. Therefore, the effect of the Ti-rich nitrides located at grain boundaries on the creep properties is neglected.

In order to determine the coherency relationship between the A2 matrix and B2 precipitates, TEM investigation was performed on a sample heat-treated at 1000 °C for 1000 h with a microstructure coarsened under similar conditions compared to the creep investigations discussed later in this article. Fig. 2(a) shows a dark-field (DF) micrograph with bright-contrast plate-like precipitates uniformly distributed throughout the matrix consistent with the SEM-BSE images shown in Fig. 1(c). The inset displays the corresponding indexed selected area electron diffraction (SAED) pattern acquired along the ⟨011⟩ zone axis from this region. The DF micrograph was obtained using a (weak) {100} superlattice spot, indicating the presence of the long-range ordered phase. The superlattice spots correspond to the B2 phase. Fig. 2(b) and (c) present atomic resolution STEM micrographs taken near the ⟨011⟩ zone axis of the matrix and precipitate, respectively. These micrographs reconfirm that the matrix and precipitates have A2 and B2 crystal structure, respectively, and exhibit $\{100\}_{A2} \parallel \{100\}_{B2}$ and $\langle001\rangle_{A2} \parallel \langle001\rangle_{B2}$ orientation relationship. The lattice parameters of the matrix a_{A2} and precipitates a_{B2} were estimated from multiple positions to be (0.323 ± 0.001) and (0.325 ± 0.001) nm, respectively. Accordingly, the misfit is confirmed positive with a relative difference in lattice parameters (see Eq. 1) of $(+ 0.6 \pm 0.4)$ %. Given the standard deviations of the measurements in A2 and B2 and the accuracy of the FFT evaluation, there is no greater precision of the difference in lattice parameters possible to this stage. It is to be noted that the local lattice parameters determined in the present case are affected by the elastic relaxation of the lattices.

3.2. Creep behavior

To understand the creep behavior of TMT-8Cr-10Al, creep tests were conducted at (1000 ± 5) °C and 125 MPa, i.e. about 50 K below the

Table 1
Composition, impurity levels and density of the homogenized TMT-8Cr-10Al.

	Composition in at. %					Impurities in wt.-ppm		Density in g·cm^{-3}
	Ta	Mo	Ti	Cr	Al	O	N	
Target	27.3	27.3	27.3	8	10	–	–	
Experimental	26.0	29.8	27.4	7.3	9.4	352 ± 88	45 ± 14	9.6

Fig. 1. Microstructure of TMT-8Cr-10Al after homogenization at 1600 °C for 20 h: (a) IPF map (color code in the inset). (b-c) SEM-BSE micrographs at different magnification.
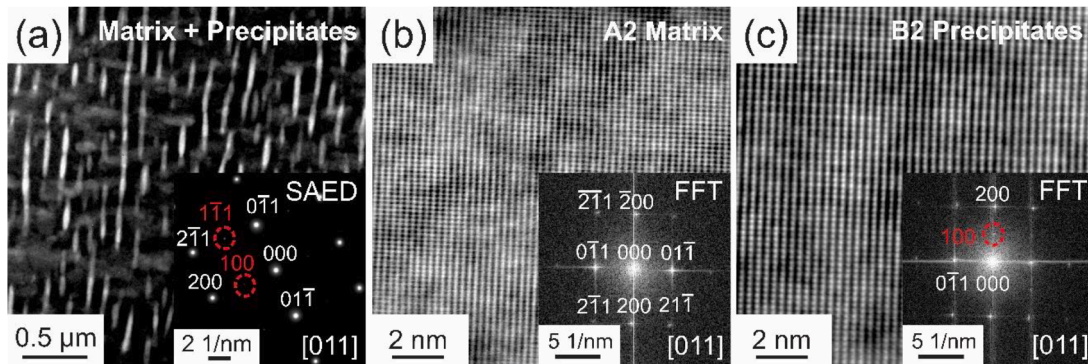
Fig. 2. TEM results on TMT-8Cr-10Al alloy after heat treatment at 1000 °C for 1000 h: (a) DF TEM micrograph showcasing bright contrast B2 precipitates uniformly distributed throughout the matrix. The micrograph was acquired using a {100} superlattice spot in the corresponding SAED pattern taken along a ⟨011⟩ zone axis from this region (inset). (b) Atomic resolution micrograph of the matrix with its corresponding FFT in the inset. (c) Atomic resolution micrograph of a B2 precipitate with its corresponding FFT in the inset.

reported solvus temperature of TMT-8Cr-10Al [27]. In order to study the relationship of creep strain with respect to time and to check its reproducibility for a precipitation-strengthened microstructure, three different creep tests under the same conditions were conducted with each test being interrupted at different strains. To study the evolution of the creep rate with increasing temperature, the creep temperature was varied between 1000 to 1060 °C, keeping the applied true stress at 125 MPa.

Fig. 3(a) shows the compression creep curves of TMT-8Cr-10Al with respect to time for total strains of 0.5 %, 0.6 % and 0.8 %. The creep rate at the end of each test was found to be approximately $2.5 \cdot 10^{-9} \, \text{s}^{-1}$. In order to visualize the creep rate for these three tests, the logarithm of creep rate vs. creep strain was plotted as shown in Fig. 3(b) with blue lines (dashes and dotted) ending in an open circle symbol. Fig. 3(b) also shows the variation of the true creep rate vs. creep strain with solid lines ending in an open circle symbol for tests at different temperatures (higher than 1000 °C) and a constant stress of 125 MPa.

It is relevant to note here that between the curves for 1000 and 1030 °C (a difference of 30 K), the minimum creep rate jumps by one order of magnitude. However, despite the smaller temperature difference between 1030 °C and 1040 °C (a difference of 10 K), the minimum creep rate also changes by one order of magnitude signifying a significant reduction in the creep resistance between 1030 and 1040 °C. This can also be observed from the values in Table 2 that the $\dot{\varepsilon}_{\text{min}}$ substantially increases (which indicates a reduction in creep resistance) between 1030 and 1040 °C. These two regions, ≤ 1030 °C and ≥ 1040 °C, are demarcated as high creep resistance (HCR) regime which exhibits a good creep resistance and the low creep resistance (LCR) regime where the creep resistance is notably lower. These two regions are highlighted by blue and red lines or symbols.

Here, a distinction has to be noted between steady state creep rate

($\dot{\varepsilon}_{\text{steady}}$) and minimum creep rate ($\dot{\varepsilon}_{\text{min}}$). In order to qualify for a mechanical [41] or even microstructural steady state [42], a substantial plastic strain release should be obtained in the period of constant strain rate. All the three tests performed at 1000 °C do not reach a steady state according to this definition. However, the creep tests performed at temperatures higher than 1000 °C reveal this steady state creep clearly. It must be noted that a steady state regime at 1000 °C could, in principle, be experimentally verified but a plastic strain release of for example 5 % would take close to 200 days. Based on the creep curve exhibiting a steady state regime at 1030 °C (full blue circle in Fig. 4), we can infer that the creep rate of $2.5 \cdot 10^{-9} \, \text{s}^{-1}$ at 1000 °C might also be regarded as the steady state creep rate. Unlike the creep curves for A1-L1$_2$ superalloys [33], the $\dot{\varepsilon}_{\text{steady}}$ observed for TMT-8Cr-10Al at all temperatures are also incidentally the $\dot{\varepsilon}_{\text{min}}$. Hence, for the discussion that follows next, we will denote the $\dot{\varepsilon}_{\text{steady}}$ as $\dot{\varepsilon}_{\text{min}}$, since both are essentially the same for TMT-8Cr-10Al alloy and it enables us to make a direct comparison to the creep behavior of other materials.

The logarithm of $\dot{\varepsilon}_{\text{min}}$ for all temperatures is plotted in Fig. 3(c) against the inverse of the temperature according to the Mukherjee-Bird-Dorn equation [43]:

$$\dot{\varepsilon}_{\text{min}} = A \frac{D_0 \, G \, b}{k \, T} \left(\frac{b}{d}\right)^p \left(\frac{\sigma}{G}\right)^n \exp\left(-\frac{Q}{R \, T}\right) \tag{2}$$

where, $\dot{\varepsilon}_{\text{min}}$ is the minimum creep rate, A the Dorn constant, D_0 a pre-exponential factor, G the shear modulus, b the Burgers vector, R the gas constant, T the temperature, d the grain size, p the inverse grain size exponent, σ the applied stress, n the stress exponent, Q the activation energy. A linear dependence is obtained.

For TMT-8Cr-10Al, two different parts of the linear fit can be observed. For each part of the Arrhenius plot, two apparent activation
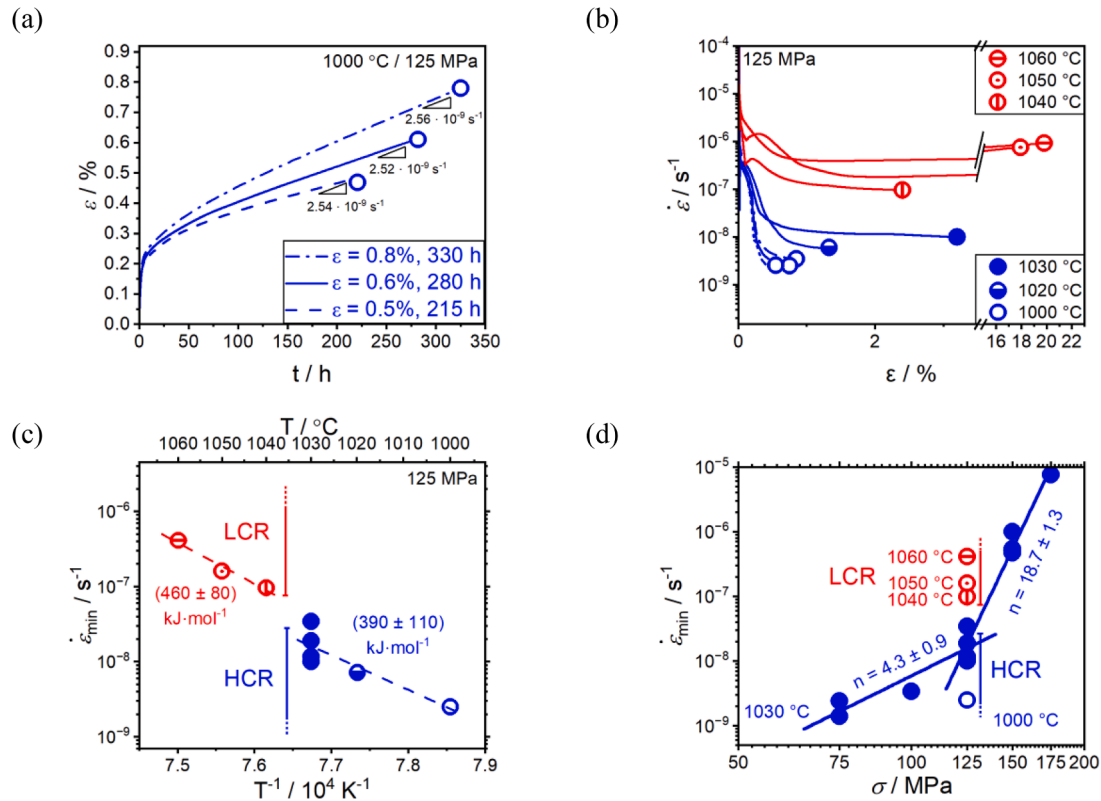
Fig. 3. Creep behavior of TMT-8Cr-10Al. The creep regimes are demarcated as high creep resistance (HCR) marked in blue and low creep resistance (LCR) depicted in red: (a) creep strain ε as a function of time t for 125 MPa and 1000 °C. (b) Logarithmic plot of creep rate $\dot{\varepsilon}$ vs. strain ε for 125 MPa at different temperatures. (c) Arrhenius plot for 125 MPa. HCR data corresponds to temperatures of 1000 °C, 1020 °C and 1030 °C, and LCR to 1040 °C, 1050 °C and 1060 °C. (d) Norton plot.

Table 2
$\dot{\varepsilon}_{\min}$ of TMT-8Cr-10Al measured at 125 MPa with different temperatures.

σ / MPa	125					
T /°C	1000	1020	1030	1040	1050	1060
$\dot{\varepsilon}_{\min}$ / s^{-1}	$2.5 \cdot 10^{-9}$	$7.1 \cdot 10^{-9}$	$1.9 \cdot 10^{-8}$	$9.6 \cdot 10^{-8}$	$1.6 \cdot 10^{-7}$	$4.1 \cdot 10^{-7}$

enthalpies (Q) can be evaluated. These two regimes incidentally also fall in the ranges of ≤1030 and ≥1040 °C, in line with the demarcation suggested for Fig. 3(b). Hence the color scheme of blue and red for ≤ 1030 and ≥1040 °C, respectively, has been maintained for Fig. 3(c). The

apparent activation energy for creep was determined to be (390 ± 110) kJ/mol in the temperature range of HCR and (460 ± 80) kJ/mol in the temperature range of LCR. Within the uncertainty range, the activation enthalpies are the same. For pure metals, a possible correlation between the apparent activation enthalpy observed during creep and the activation enthalpy for the self-diffusion of the metal atoms was reported valid [44]. However, this straightforward correlation becomes difficult when multi-component, single-phase or even multi-phase materials are addressed [45]. Considering that TMT-8Cr-10Al not only has five principal elements but also two different phases along with grain boundaries, the correlation of the obtained activation enthalpy for creep with the activation enthalpy for the self-diffusion of the constituent elements
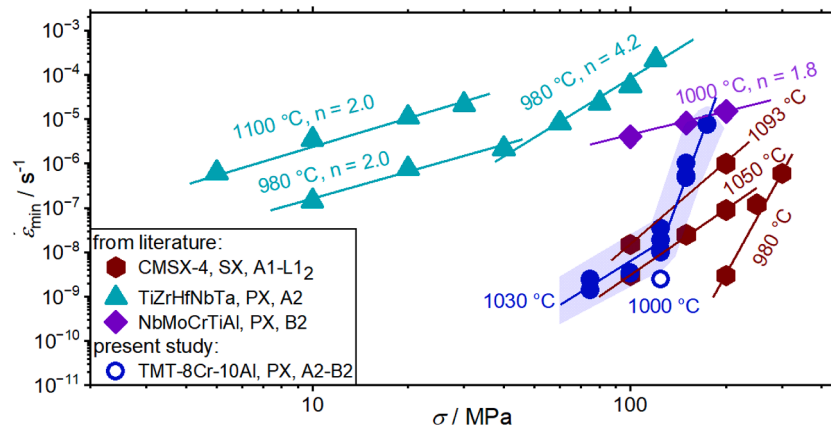
Fig. 4. Comparison of minimum or steady state strain rate vs. applied stress for the investigated polycrystalline (PX), A2+B2 TMT-8Cr-10Al alloy and PX, single-phase B2 NbMoCrTiAl alloy [50], PX, single-phase A2 TiZrHfNbTa [29] as well as for the single-crystalline (SX) Ni-based superalloy CMSX-4 with A1-L1$_2$ microstructure.

is not trivial.

In order to determine the apparent stress exponent n according to Eq. (2) [43], creep tests were conducted at 1030 °C at three different stresses ranging from 75 to 175 MPa. The results are shown in Fig. 3(d). The n value is determined by plotting the logarithm of minimum creep rate at constant temperature against the different applied stresses. The apparent stress exponent n determined by linear fitting is (4.3 ± 0.9) for the low stress regime between 75 to 125 MPa. When compared to pure metals and single-phase alloys, n values between 3 and 5 indicate dislocation climb as the rate controlling process of creep [46]. It should be noted that similar to the activation enthalpy discussed earlier, the evaluated n is an apparent quantity. This is due to the fact that the observed creep behavior is an effective behavior potentially involving several fundamental mechanisms in TMT-8Cr-10Al, such as dislocation glide and climb. Similar to the activation enthalpy, a simple comparison to single-phase metals or alloys might lead to a false conclusion without proper microstructural evidence for the active micromechanical mechanisms. For stresses beyond 125 MPa, $n = (18.7 \pm 1.3)$ is obtained indicating the onset of a power law break down.

For the present samples, grain sizes are rather coarse specifically when considering the sample size used in the creep tests. In order to verify the relevance of the tests, various tests were repeated with a specific emphasis on 1030 °C as a wide stress range was possible to be captured. These repetitions prove the relevance of the test data. While in A1-L1$_2$ alloys, resistance to creep is significantly dependent on the loading direction [47], the potential higher multiplicity of slip systems in A2-based systems leads to lower variation of resolved shear stress and thus less anisotropy of the creep response. The results on the coarse-grained material presented here are consistent with this assumption.

For a precipitation-strengthened material like TMT-8Cr-10Al, it is imperative to compare the macro-mechanical properties like creep with other high temperature alloys. Fig. 4 shows the creep results of polycrystalline TMT-8Cr-10Al consisting of A2 matrix and B2 precipitates as compared to those of single-crystal Ni-based superalloy CMSX-4 with A1 matrix and L1$_2$ precipitates [48,49], polycrystalline single-phase, A2 TiZrHfNbTa [29] and single-phase B2 NbMoCrTiAl [50]. The minimum creep rates at low stresses of 75 to 125 MPa of polycrystalline TMT-8Cr-10Al at 1030 °C are comparable to those of single-crystalline CMSX-4 at 1050 °C and similar stresses as can be seen in Fig. 4. It must be noted that TMT-8Cr-10Al tested at 1030 °C is operated much closer to the reported solvus temperature of the B2 precipitates (T_S) of 1055 °C (0.98 T_S, see the discussion of Fig. 8 below for the actual solvus temperature of 1060 to 1070 °C corresponding to 0.97 T_S) compared to the case of CMSX-4 tested at 1050 °C with a solvus temperature of L1$_2$ of 1280 °C (0.85 T_S). At comparable temperatures and stresses, TMT-8Cr-10Al has a minimum creep rate about four orders of magnitude lower than both the single-phase A2 TiZrHfNbTa alloy and the single-phase B2 NbMoCrTiAl alloy, which undergoes a microstructural decomposition to a multi-phase intermetallic microstructure during creep [50]. This reaffirms the substantial impact of precipitation strengthening achieved in TMT-8Cr-10Al.

3.3. Microstructure evolution after creep deformation

Fig. 5(a–c) shows the SEM-BSE micrographs and the evolution of TMT-8Cr-10Al after creep deformation at 1000 °C/125 MPa for strains of 0.5, 0.6, and 0.8 %, respectively. The compression direction in the micrographs is horizontal. In the absence of creep deformation, the size of the B2 precipitates were previously reported to increase with increasing heat treatment times while the phase fraction of the precipitates was found to initially increase (the growth regime) before saturating after a certain annealing time (the coarsening regime) [28]. To illustrate the difference in the microstructure after annealing without creep deformation, samples were heat treated at 1000 °C for times equivalent to each creep test, as displayed in Fig. 5(d-f).

Fig. 6 depicts the changes in phase fraction of the precipitates at 1000 °C after creep and heat treatment for the different times and microstructures as revealed in Fig. 5. The increase in the phase fraction of the precipitates (calculated by area fraction in the SEM-BSE images) is evident in both the crept and annealed samples. The phase fraction of precipitates increases over the tested time range, which indicates that the precipitates are still in the process of growth during the creep deformation as opposed to being in the coarsening process where a saturation of the precipitate fraction is expected. Furthermore, it can be seen from Fig. 6 that the precipitate growth is accelerated under creep
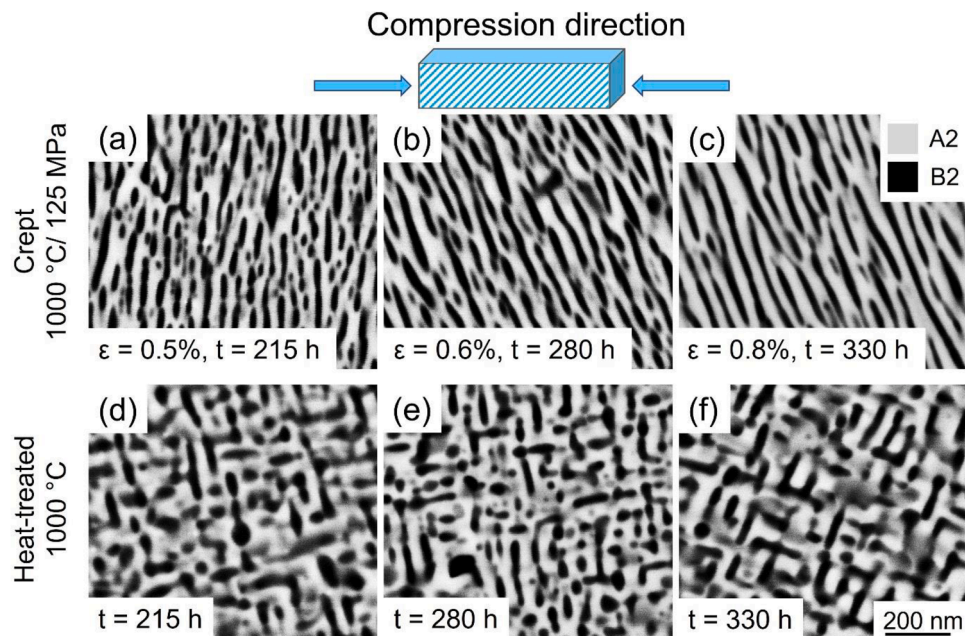
Fig. 5. SEM-BSE micrographs showing microstructure evolution of TMT-8Cr-10Al alloy after creep tests at 1000 °C with a stress of 125 MPa and strains of: (a) 0.5 %, (b) 0.6 %, and (c) 0.8 % as well as heat treatments at 1000 °C for: (d) 215 h, (e) 280 h, and (f) 330 h. The grains in the crept condition are selected to visualize the rafting. See Fig. 7 for the orientation dependence of rafting.
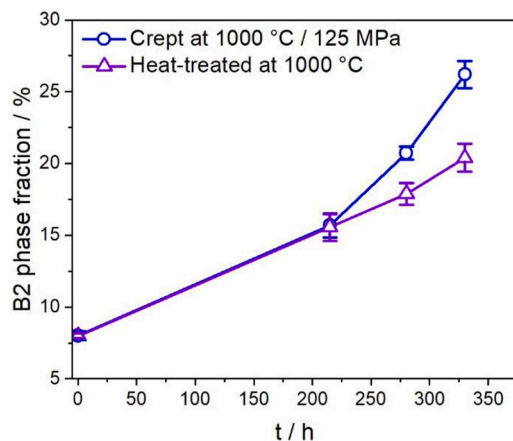
Fig. 6. The phase fraction of B2 precipitates of TMT-8Cr-10Al at 1000 °C as a function of time of creep deformation (125 MPa) and annealing.

Fig. 7. EBSD-IPF maps and the direction of rafting (1–4) in each corresponding grain. The creep tests were performed at 1000 °C for total strains of (a) 0.5 % and (b) 0.8 %.

conditions as compared to the conditions without plastic deformation imposed. The impact of additional deformation on the kinetics of precipitate growth can be attributed to the dislocation activity. Dislocations might act as heterogeneous nucleation sites as well as fast diffusion paths enhancing both the nucleation and growth rates, respectively.

Besides the change in the fraction of the precipitates, the other notable difference between the crept and the annealed samples is in the morphology of the precipitates. In contrast to the heat-treated samples, the crept microstructures show a pronounced directional growth similar to the rafting phenomenon of precipitates in Al-L1$_2$ Ni-based superalloys. As mentioned earlier, the majority of the creep experiments on Al-L1$_2$ Ni-based superalloys were performed on $\langle 100 \rangle$ oriented single crystals. Since the samples used in the present study are polycrystalline, the correlation between the grain orientation, and the angle between the loading direction to the rafted precipitates is not straightforward. In order to study such a correlation, EBSD investigations were performed on samples crept at 1000 °C up to a strain of 0.5 % (Fig. 7(a)) and 0.8 % (Fig. 7(b)). The relationship between the loading direction and the surface on which EBSD was performed is illustrated in Fig. 7. The color code corresponds to the inverse pole figure of the compression direction in the inset. A few grains in the IPF map for each sample in Fig. 8 are selected (marked 1–4) to represent the orientations close to the corners of the standard triangle. The SEM-BSE images highlighting the rafting direction for the grains marked in Fig. 7(a) and (b) are shown in Fig. 7 (a1) to (a4) and (b1) to (b4), respectively.

As was summarized in Table S1 of the Supplementary Material, N-type rafting is observed when the sign of lattice misfit (+ / −) is opposite to the loading type, e.g. compression (−)/tension (+). For the present case, this was verified as the lattice misfit of the B2 precipitates was observed to be positive (+) via HR-TEM in Fig. 2(b-c) and compression (−) was applied during creep. Two observations in this regard are important to conclude from Fig. 7. Firstly, the direction of rafting with respect to the compression direction is not unique and strongly depends on the grain orientation. Secondly, the direction of rafting is clearly perpendicular to the compression direction for the grains where a $\langle 100 \rangle$ direction is parallel to the compression direction. This observation is similar to the creep results in polycrystalline Co-based superalloys, where rafting perpendicular to the compression direction was observed only for $\langle 100 \rangle$ oriented grains [36,51]. The angles between the rafted structure and the loading direction lie between 45 to 70° in grain orientations other than $\langle 100 \rangle$. Thus, it can be concluded that similar to the A1-L1$_2$ Ni- and Co-based superalloys, the direction of the rafted microstructure can be predicted following the same scheme as presented in Table S1 in the Supplementary Material for grains whose $\langle 100 \rangle$ are close or even parallel to the compression direction.

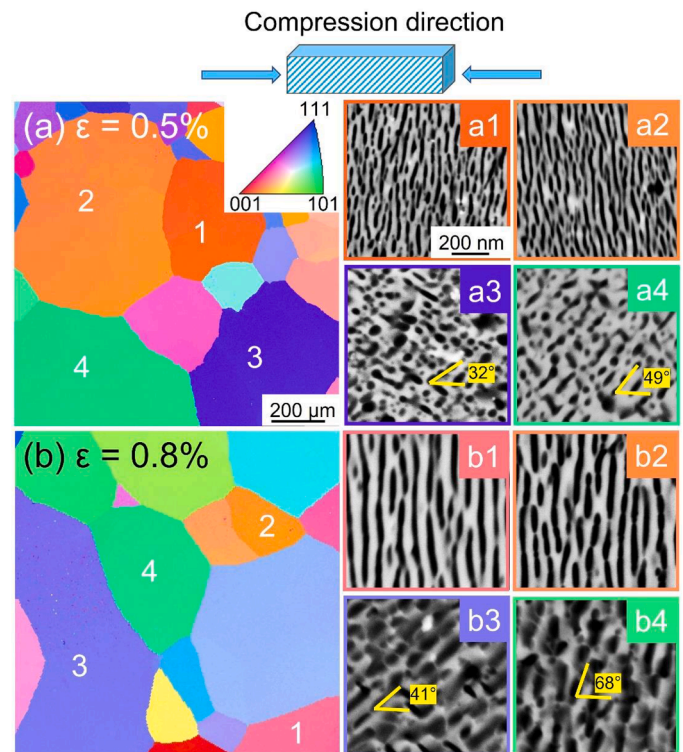In the present case, a steady-state creep rate is obtained (see Section

3.3) while substantial mesoscopic microstructural changes occur. This might be rationalized by the differentiation of mechanical and microstructural steady state as stressed earlier by Mughrabi [42]. Steady-state creep rate is a result of a time-dependent balance of strengthening and softening contributions during creep. The assessment of the various potential contributions is complex for the present case as dislocation strengthening, dislocation annihilation, precipitation strengthening (dislocation-particle interaction) and solid solution strengthening are active at the same time. Qualitatively, B2 precipitation during creep deformation might contribute to a strengthening (decreasing creep rate) while the depletion of the precipitating elements might significantly reduce the solid solution strengthening in the A2 matrix (increasing creep rate). As a concentrated solid solution matrix is considered here, this aspect might be more pronounced as in other engineering alloys. Local minima and variations in the slopes of the creep curves (see Fig. 3 (b)), as for example obtained in the early stages of creep at 1040 to 1060 °C, might indicate also transitions between different stages of creep mechanisms. This is subject of ongoing investigations with interrupted creep tests.

Since a significant reduction of creep resistance was obtained at temperatures $\geq$ 1040 °C (LCR in Fig. 3) with increasing temperature as shown in Fig. 3(b), it is required to correlate the evolution of microstructure in the creep samples at higher temperatures. Fig. 8(a–c) shows the microstructural evolution of crept samples at temperatures ranging from 1030 to 1060 °C at a constant stress of 125 MPa.

The microstructural features after creep at 1030 °C are quite similar to those at 1000 °C in terms of rafting of the precipitates. In contrast, the microstructure for sample crept at 1040 °C and higher appears different. The microstructure of the sample crept at 1060 °C, shows a much smaller rafted length as compared to the sample crept at 1030 °C, even though the total strain is over six times larger. It must be noted however that the creep time for each temperature condition is not the same. The samples for the microstructure Fig. 8(a–c) were cooled inside the furnace after the completion of the creep experiments. This furnace
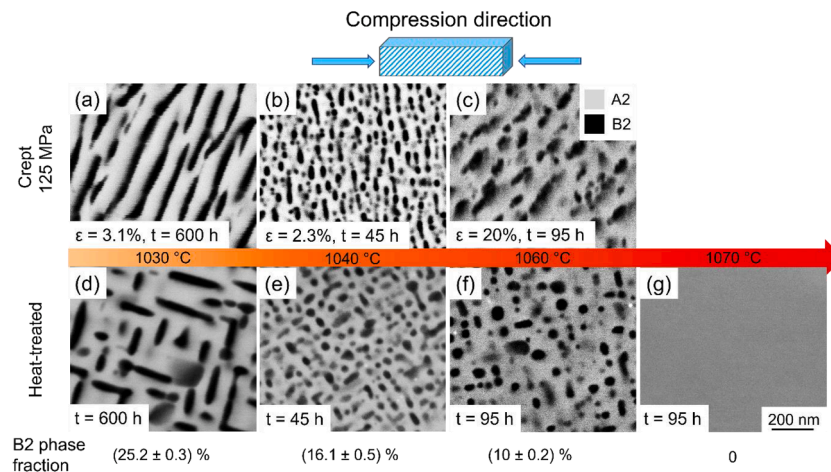
Fig. 8. Microstructure evolution of TMT-8Cr-10Al alloy after creep tests and heat treatments: (a) 1030 °C/125 MPa/3.1 %, (b) 1040 °C/125 MPa/2.3 %, (c) 1060 °C/125 MPa/20 %. (d) 1030 °C/600 h, (e) 1040 °C/45 h, (f) 1060 °C/95 h and (g) 1070 °C/95 h. Same magnification used in all images.

cooling allows the precipitates to re-nucleate during the cooling process. Thus, the microstructures shown in Fig. 8(a–c) may not depict the actual state of the samples during the creep experiments. Therefore, samples were additionally heat-treated at the same temperature and for the same time as in the creep test and then quenched in water in order to compare the microstructure in the stressed and stress-free states. These micrographs are shown in Fig. 8(d–g). Note that the heat-treated samples were placed in an ampoule, heated to the target temperature for a specified time, and then quenched. In contrast, the creep samples were slowly cooled down in the creep testing setup due to the technical requirements of the furnace. Therefore, the microstructure observed in the creep samples does not reflect the condition when the creep test was terminated. At 1060 °C, the samples still contain B2 precipitates after being annealed for 95 h. In order to determine the temperature where the precipitates dissolve completely, one sample was also annealed at 1070 °C for 95 h (similar to the time for 1060 °C) wherein no precipitates were found (Fig. 8(g)). It should be further noted that although 1060 °C (Fig. 8(f)) is slightly higher than the previously reported solvus temperature of 1055 °C for B2 in TMT-8Cr-10Al, B2 precipitates still appear. Single-phase A2 devoid of B2 precipitates in TMT-8Cr-10Al is only verified for 1070 °C in these additional annealing experiments. There are many aspects, which can explain this deviation. Firstly, the determination of the solvus temperature in Ref. [27] involves the analysis of the peak temperature of the heat signature in the DSC experiment. However, the formation of the present microstructure involves two reaction types, e.g. a diffusion-controlled 1st order phase separation as well as a 2nd order, solid-state ordering reaction [27]. The heat signatures of both are superimposed in the DSC experiments. While 2nd order transitions are indeed evaluated for their characteristic peak temperatures [52], diffusion-controlled 1st order phase transformations need to be characterized by their extrapolated peak-onset temperatures [52–55]. As the lambda-shaped heat signature of the 2nd order phase transformation spans down to 800 °C in the case of TMT-8Cr-10Al, the onset of the diffusion-controlled characteristic temperatures of the 1st order phase separation can only be estimated from DSC experiments by the evaluation of the peak temperature. Secondly, it is important to consider that the dissolution of the precipitates is a diffusion-controlled process, hence the dissolution of the precipitates beyond the solvus temperature is also dependent on the time of annealing. Taking these two aspects into account in addition to the possible errors in the different thermocouples used in the DSC and furnaces used for annealing and in the creep testing device, it is reasonable to state that the actual solvus temperature is very close to the previously reported solvus temperature of 1055 °C with a possible difference of around 10 K.

Although B2 precipitates were observed up to annealing tempera-

tures of 1060 °C, not just the presence of precipitates but also the phase fraction of the precipitates plays a key role in determining the creep response of the TMT-8Cr-10Al. Since, the annealing times for Fig. 8(d–g) are not constant, additional annealing treatments were conducted at 1040 °C and 1050 °C for 95 h in order to quantitatively analyze the temperature depending volume fraction of the precipitates. These results are plotted in Fig. 9. It is clear that although the precipitates are still present at 1060 °C, the volume fraction decreases sharply from 1040 °C. Based on the chemical compositions of A2 and B2 reported earlier [28], the maximum volume fraction amounts to 13 to 18 vol. % depending on assumption of the re-calculation. The higher $\dot{\varepsilon}_{min}$ observed in the LCR regime (Fig. 3(b)) is, hence, mainly caused by a reduction in the B2 phase fraction at temperatures close to the actual solvus temperature. It is relevant to note that creep tests at 125 MPa in the single-phase A2 region $\geq$ 1070 °C repeatedly failed by too fast creep rates. Apart from benefits of the creep performance of TMT-8Cr-10Al over polycrystalline A2, polycrystalline B2 and also single-crystalline CMSX-4 as showcased in Section 3.2, the relevance of precipitation strengthening for causing these excellent creep properties is highlighted by these observations.

Despite the advancements in our current alloy system, the solvus temperature of the B2 precipitates remains limited. This constraint highlights the pressing necessity to develop new RCCAs with substantially higher solvus temperatures, allowing operation beyond the limits of conventional Ni-based superalloys. Recent studies [56–58] have identified the potential of Ru-based B2 strengthening phases, particularly the HfRu-B2 phase. It is notable that this phase exhibits remarkable stability at temperatures up to 1900 °C combined with minimal lattice
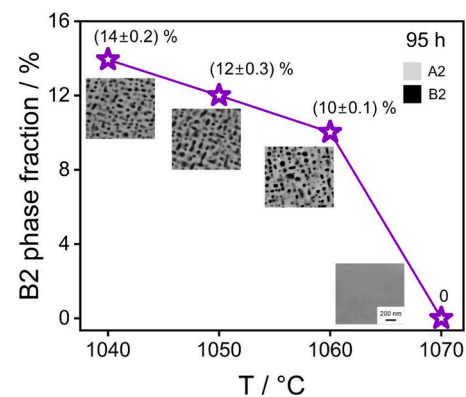
Fig. 9. The phase fraction of B2 precipitates of TMT-8Cr-10Al annealed at 1040 °C to 1070 °C for 95 h. Same magnification used in all images.

misfit. These attributes position HfRu-B2 as a highly promising candidate for strengthening precipitates, providing a path for the development of RCCAs with higher solvus temperature and substantially improved creep resistance. This might be of great engineering relevance in view of potentially negative aspects and challenges in the application of RCCAs, like higher costs and more complex processing, or properties not yet met in sufficient manner, like density, oxidation resistance, etc. which require further development efforts.

3.4. Strengthening contribution of B2 precipitates

The Lagneborg-Bergman-Reppich (LBR) method [59–61] was originally developed for precipitation strengthened alloys to determine the contribution of precipitates to the overall creep strength of the alloys. This method is also applicable to A2+B2 TMT-8Cr-10Al. As the deformation of the precipitation-strengthened alloy may mostly be carried by the A2 matrix phase, the effective stress σ required to maintain a specific minimum creep rate $\dot{\varepsilon}_{\min}$ is assumed as the sum of the stress that would generate the same creep rate in the single-phase A2 matrix σ_{A2} and the strengthening contribution from the precipitates σ_{B2}, e.g. $\sigma = \sigma_{A2} + \sigma_{B2}$. A simplified form of Eq. (2) in Section 3.2 for the temperature and stress dependence of $\dot{\varepsilon}_{\min}$ then reads

$$\dot{\varepsilon}_{\min} = B \left(\sigma_{A2} + \sigma_{B2} \right)^{n_{A2}} \exp\left(-\frac{Q_{A2}}{R\,T} \right) \tag{3}$$

with n_{A2} and Q_{A2} being the apparent stress exponent and activation enthalpy of the A2 matrix. B is a materials constant. In general, σ_{B2} exhibits a characteristic dependence on the applied stress [59], e.g. increasing in the low stress regime, becoming a constant (maximum) value at high stresses. Considering a sinh-type stress dependence of $\dot{\varepsilon}_{\min}$ allows to account for the stress dependence of $n_{A2}(\sigma)$ in the LBR method in its recent form by plotting the creep response of A2 as well as of the A2+B2 precipitation-strengthened material in a $\dot{\varepsilon}_{\min}^{1/n_{A2}(\sigma)}$ vs. σ plot.

In the case of traditional Ni- or Co-based superalloys, determining the contribution of L1$_2$ precipitates in the two-phase microstructure requires synthesizing the single-phase A1 matrix alloy based on the A1 matrix composition. This approach is necessary because the creep test temperature often significantly differs from the solvus temperature of this type of superalloy. For TMT-8Cr-10Al, the actual solvus temperature is confirmed to be between 1060 °C and 1070 °C, see context of Figs. 8 and 9, which is close to the test temperature range of the HCR regime (see Fig. 3(d)), e.g. 1000 to 1030 °C. The creep resistance of the single-phase A2 matrix alloy was assessed by testing under varying applied stresses at 1070 °C, a temperature where the alloy stays within the A2 single-phase condition. The data of these tests is compiled in Fig. 10(a) as full red circles.

The LBR approach can be applied when the following two assumptions are made: (i) The difference in chemical composition between the alloy composition (and, thus the composition of the A2 phase tested at 1070 °C) and the actual A2 matrix in the two-phase microstructure does not lead to substantial differences in the minimum creep rate. (ii) The consistent trend in thermal activation of creep for 125 MPa in the entire temperature range tested (see Fig. 3(c)) is valid also for other stresses.

The confirmation of assumption (i) requires the synthesis of monolithic A2 of the correct composition, which will be subject of future investigations. However, slightly lower minimum creep rates are to be expected as a consequence of a higher solidus temperature of the actual A2 matrix due to the enrichment in Ta and Mo over the alloy composition. The estimated creep resistance of the single-phase A2 matrix at 1030 °C recalculated using Eq. (2) is indicated by the orange five-pointed star symbols in Fig. 10(a). The shaded region indicates differences in activation enthalpy as determined for HCR and LCR in Fig. 3(c). Thus, assumption (ii) might only negligibly affect the evaluation here.

From this representation an advancement of about 45 MPa of the A2+B2 condition is obtained at 10^{-8} s^{-1} minimum creep rate. In order to account for the stress dependence of the apparent stress exponent $n_{A2}(\sigma)$ (2.5 to 6.6 between 50 and 125 MPa), $\dot{\varepsilon}_{\min}^{1/n_{A2}(\sigma)}$ vs. σ is plotted in Fig. 10(b). The physical strengthening contribution by the precipitates is then only $\sigma_{A2} \approx 15$ MPa for the same strain rate of 10^{-8} s^{-1}.
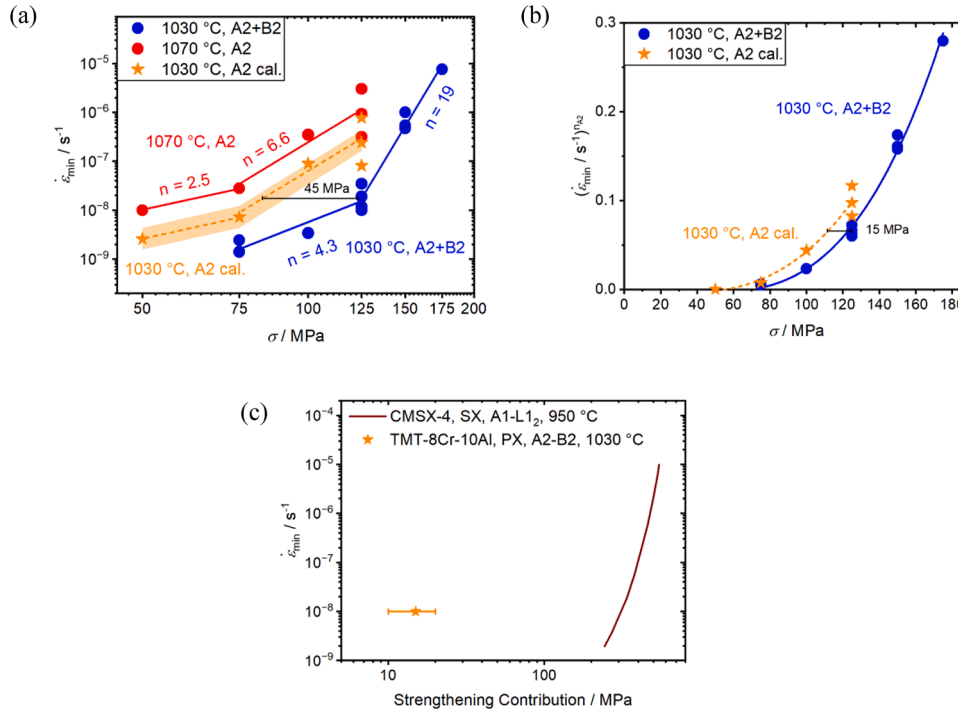
Fig. 10. (a) Norton plot with a comparison of minimum creep rates of A2 and A2+B2. The data of A2 was recalculated to 1030 °C using the thermal activation data presented in Fig. 3(c). (b) LBR plot with $\dot{\varepsilon}_{\min}^{1/n_{A2}(\sigma)}$ vs. σ to deduce σ_{A2}, (c) Precipitation strengthening contributions at 1030 and 950 °C of TMT-8Cr-10Al in comparison to CMSX-4 [59,62], respectively.

[Fig. 10](c) compares the precipitation strengthening contribution of the TMT-8Cr-10Al with that of the Ni-based superalloy CMSX-4 [59,62], however, due to the limited available data only for very different temperatures of 1030 °C in the case of the RCCA and 950 °C in the case of the superalloy. It is obvious that the strengthening contribution by B2 is low in the RCCA. With respect to the volume fraction, Ref. [59] highlights a significant dependence as a reduction of volume fraction from 70 to 20 % leads to a linear drop of the strengthening contribution from about 300 MPa to substantially below 100 MPa in Co-based superalloys. Consequently, it is not surprising that the B2 precipitates in TMT-8Cr-10Al with a significantly lower volume fraction compared to Ni-based superalloy CMSX-4 result in a much lower strengthening contribution. The test temperatures being very close to the solvus temperature in the present situation further decreases the precipitation strengthening contribution in TMT-8Cr-10Al compared to the data of CMSX-4. The fact that the creep strengths of TMT-8Cr-10Al and the Ni-based superalloy CMSX-4 are nevertheless at a similar level shows the great potential of the precipitation-strengthened A2-B2 TMT-8Cr-10Al alloy system, provided that the precipitate fraction and solvus temperature can still be increased.

5. Conclusions

The polycrystalline refractory high entropy alloy 27.3Ta-27.3Mo-27.3Ti-8Cr-10Al (at. %, TMT-8Cr-10Al) with a two-phase microstructure consisting of a disordered A2 matrix and ordered B2 precipitates shows a promising creep resistance at high temperatures.

Compared to polycrystalline, single-phase A2 and B2 RHEAs, it can be concluded that

- The precipitation-strengthened TMT-8Cr-10Al exhibits a substantially higher creep resistance over other single-phase, polycrystalline A2 and B2 RHEAs. The difference amounts to about three to four orders of magnitude in creep rate at comparable stresses and temperatures.

Compared to state-of-the-art, single-crystalline A1-L1$_2$ CMSX-4, it can be concluded that

- TMT-8Cr-10Al possesses a comparable minimum creep rate compared to CMSX-4 in the stress range of 75 to 125 MPa and temperatures ranging from 1000 to 1030 °C.
- The comparable creep resistance under these testing conditions is remarkable as TMT-8Cr-10Al is polycrystalline compared to the single-crystalline CMSX-4. At 1030 °C, TMT-8Cr-10Al is tested much closer to its solvus temperature of 1060 to 1070 °C compared to CMSX-4 with 1280 °C solvus temperature.
- Due to close proximity to the solvus temperature during testing and comparably low volume fraction of B2, the B2 strengthening contribution under creep condition remains considerably smaller compared to state-of-the-art Ni-base superalloys. Therefore, the targets for future alloy developments should be an increase in solvus temperature and volume fraction of the B2 precipitates.
- The further, guided development of Ta-Mo-Ti-Cr-Al+X RCCA with improved precipitate volume fraction and solvus temperature requires improvements of the currently existing thermodynamic models, for example like presented in Ref. [63], as the relevant temperatures of phase separation and ordering are not well captured by simulations so far [27,28].

Regarding the microstructural changes upon creep and annealing, the following conclusions can be drawn:

- A directional coarsening or rafting of precipitates microstructure of TMT-8Cr-10Al is observed after creep at 1000 and 1030 °C with a stress of 125 MPa. The combination of positive lattice misfit and compression loading causes N-type rafting of the microstructure in grains with ⟨100⟩ parallel to the loading direction consistent with the established theories on the formation of rafted microstructures in Ni- and Co-based superalloys.
- The reduction in the creep resistance observed at higher temperatures of 1040, 1050 and 1060 °C close to the solvus temperature is correlated to a significant reduction of the B2 phase fraction.

Prime novelty statement

We confirm that this manuscript has not been published previously by any of the authors and is not under consideration for publication in another journal.

CRediT authorship contribution statement

Liu Yang: Writing – review & editing, Writing – original draft, Visualization, Validation, Project administration, Investigation, Funding acquisition, Formal analysis, Data curation. **Sandipan Sen:** Writing – review & editing, Writing – original draft, Visualization, Validation, Supervision, Project administration, Methodology, Investigation, Formal analysis, Data curation, Conceptualization. **Daniel Schliephake:** Writing – review & editing, Methodology, Investigation, Data curation. **R. J. Vikram:** Writing – review & editing, Writing – original draft, Visualization, Supervision, Methodology, Investigation, Formal analysis, Data curation, Conceptualization. **Stephan Laube:** Writing – review & editing, Investigation. **Aparajita Pramanik:** Writing – review & editing, Visualization, Methodology, Investigation. **Ankur Chauhan:** Writing – review & editing, Visualization, Supervision, Methodology, Investigation. **Steffen Neumeier:** Conceptualization, Formal analysis, Writing – review & editing. **Martin Heilmaier:** Writing – review & editing, Supervision, Funding acquisition, Conceptualization. **Alexander Kauffmann:** Writing – review & editing, Writing – original draft, Visualization, Supervision, Methodology, Formal analysis, Conceptualization.

Declaration of competing interest

The authors declare that they have no known competing financial interests or personal relationships that could have appeared to influence the work reported in this paper.

Data availability statement

The data presented in this study are available in KITopen at https://doi.org/10.35097/ehrvgc6vyb7exqcs under CC BY-SA 4.0 license. Further information is available upon request with alexander.kauffmann@kit.edu.

Supplementary materials

Supplementary material associated with this article can be found, in the online version, at doi:10.1016/j.actamat.2025.120827.

References

[1] J.-W. Yeh, S.-K. Chen, S.-J. Lin, J.-Y. Gan, T.-S. Chin, T.-T. Shun, C.-H. Tsau, S.-Y. Chang, Nanostructured high-entropy alloys with multiple principal elements: novel alloy design concepts and outcomes, Adv. Eng. Mater. 6 (2004) 299–303, https://doi.org/10.1002/adem.200300567.

[2] J.-W. Yeh, S.-J. Lin, T.-S. Chin, J.-Y. Gan, S.-K. Chen, T.-T. Shun, C.-H. Tsau, S.-Y. Chou, Formation of simple crystal structures in Cu-Co-Ni-Cr-Al-Fe-Ti-V alloys with multiprincipal metallic elements, Metall. Mater. Trans. A 35 (2004) 2533–2536, https://doi.org/10.1007/s11661-006-0234-4.

[3] B. Cantor, I.T.H. Chang, P. Knight, A.J.B. Vincent, Microstructural development in equiatomic multicomponent alloys, Mater. Sci. Eng. A 375–377 (2004) 213–218, https://doi.org/10.1016/j.msea.2003.10.257.

[4] O.N. Senkov, G.B. Wilks, D.B. Miracle, C.P. Chuang, P.K. Liaw, Refractory high-entropy alloys, Intermetallics. (Barking) 18 (2010) 1758–1765, https://doi.org/10.1016/j.intermet.2010.05.014.

[5] O.N. Senkov, G.B. Wilks, J.M. Scott, D.B. Miracle, Mechanical properties of Nb25Mo25Ta25W25 and V20Nb20Mo20Ta20W20 refractory high entropy alloys, Intermetallics (Barking) 19 (2011) 698–706, https://doi.org/10.1016/j.intermet.2011.01.004.

[6] O.N. Senkov, J.M. Scott, S.V. Senkova, D.B. Miracle, C.F. Woodward, Microstructure and room temperature properties of a high-entropy TaNbHfZrTi alloy, J. Alloys. Compd. 509 (2011) 6043–6048, https://doi.org/10.1016/j.jallcom.2011.02.171.

[7] O.N. Senkov, J.M. Scott, S.V. Senkova, F. Meisenkothen, D.B. Miracle, C.F. Woodward, Microstructure and elevated temperature properties of a refractory TaNbHfZrTi alloy, J. Mater. Sci. 47 (2012) 4062–4074, https://doi.org/10.1007/s10853-012-6260-2.

[8] B. Gorr, S. Schellert, F. Müller, H.-J. Christ, A. Kauffmann, M. Heilmaier, Current status of research on the oxidation behavior of refractory high entropy alloys, Adv. Eng. Mater. 23 (2021) 2001047, https://doi.org/10.1002/adem.202001047.

[9] B. Gorr, M. Azim, H.-J. Christ, T. Mueller, D. Schliephake, M. Heilmaier, Phase equilibria, microstructure, and high temperature oxidation resistance of novel refractory high-entropy alloys, J. Alloys. Compd. 624 (2015) 270–278.

[10] B. Gorr, F. Müller, M. Azim, H.-J. Christ, T. Müller, H. Chen, A. Kauffmann, M. Heilmaier, High-temperature oxidation behavior of refractory High-entropy alloys: effect of alloy composition, Oxid. Met. 88 (2017) 339–349, https://doi.org/10.1007/s11085-016-9696-y.

[11] C.M. Liu, H.M. Wang, S.Q. Zhang, H.B. Tang, A.L. Zhang, Microstructure and oxidation behavior of new refractory high entropy alloys, J. Alloys. Compd. 583 (2014) 162–169.

[12] S. Schellert, B. Gorr, S. Laube, A. Kauffmann, M. Heilmaier, H.J. Christ, Oxidation mechanism of refractory high entropy alloys Ta-Mo-Cr-Ti-Al with varying Ta content, Corros. Sci. 192 (2021) 109861, https://doi.org/10.1016/j.corsci.2021.109861.

[13] B. Gorr, F. Müller, S. Schellert, H.-J. Christ, H. Chen, A. Kauffmann, M. Heilmaier, A new strategy to intrinsically protect refractory metal based alloys at ultra high temperatures, Corros. Sci. 166 (2020) 108475, https://doi.org/10.1016/j.corsci.2020.108475.

[14] S. Schellert, B. Gorr, H.-J. Christ, C. Pritzel, S. Laube, A. Kauffmann, M. Heilmaier, The effect of Al on the formation of a CrTaO4 layer in refractory high entropy alloys Ta-Mo-Cr-Ti-xAl, Oxid. Met. 96 (2021) 333–345, https://doi.org/10.1007/s11085-021-10046-7.

[15] S. Schellert, M. Weber, H.J. Christ, C. Wiktor, B. Butz, M.C. Galetz, S. Laube, A. Kauffmann, M. Heilmaier, B. Gorr, Formation of rutile (Cr,Ta,Ti)O2 oxides during oxidation of refractory high entropy alloys in Ta-Mo-Cr-Ti-Al system, Corros. Sci. 211 (2023) 110885, https://doi.org/10.1016/j.corsci.2022.110885.

[16] H. Chen, A. Kauffmann, B. Gorr, D. Schliephake, C. Seemüller, J.N. Wagner, H.-J. Christ, M. Heilmaier, Microstructure and mechanical properties at elevated temperatures of a new Al-containing refractory high-entropy alloy Nb-Mo-Cr-Ti-Al, J. Alloys. Compd. 661 (2016) 206–215.

[17] H. Chen, A. Kauffmann, S. Laube, I.-C. Choi, R. Schwaiger, Y. Huang, K. Lichtenberg, F. Müller, B. Gorr, H.-J. Christ, M. Heilmaier, Contribution of lattice distortion to solid solution strengthening in a series of refractory high entropy alloys, Metall. Mater. Trans. A 49 (2018) 772–781, https://doi.org/10.1007/s11661-017-4386-1.

[18] H. Chen, A. Kauffmann, S. Seils, T. Boll, C.H. Liebscher, I. Harding, K.S. Kumar, D.V. Szabó, S. Schlabach, S. Kauffmann-Weiss, F. Müller, B. Gorr, H.-J. Christ, M. Heilmaier, Crystallographic ordering in a series of Al-containing refractory high entropy alloys Ta–Nb–Mo–Cr–Ti–Al, Acta Mater. 176 (2019) 123–133, https://doi.org/10.1016/j.actamat.2019.07.001.

[19] S. Laube, H. Chen, A. Kauffmann, S. Schellert, F. Müller, B. Gorr, J. Müller, B. Butz, H.-J. Christ, M. Heilmaier, Controlling crystallographic ordering in Mo–Cr–Ti–Al high entropy alloys to enhance ductility, J. Alloys. Compd. 823 (2020) 153805, https://doi.org/10.1016/j.jallcom.2020.153805.

[20] S. Laube, G. Winkens, A. Kauffmann, J. Li, C. Kirchlechner, M. Heilmaier, Strength of disordered and ordered Al-containing refractory high-entropy alloys, Adv. Eng. Mater. (2024) 2301797, https://doi.org/10.1002/adem.202301797.

[21] D.B. Miracle, M.-H. Tsai, O.N. Senkov, V. Soni, R. Banerjee, Refractory high entropy superalloys (RSAs), Scr. Mater. 187 (2020) 445–452, https://doi.org/10.1016/j.scriptamat.2020.06.048.

[22] D.-M. Jin, Z.-H. Wang, J.-F. Li, B. Niu, Q. Wang, Formation of coherent BCC/B2 microstructure and mechanical properties of Al–Ti–Zr–Nb–Ta–Cr/Mo light-weight refractory high-entropy alloys, Rare Met. 41 (2022) 2886–2893, https://doi.org/10.1007/s12598-022-01971-w.

[23] N. Yurchenko, E. Panina, D. Shaysultanov, S. Zherebtsov, N. Stepanov, Refractory high entropy alloy with ductile intermetallic B2 matrix/hard bcc particles and exceptional strain hardening capacity, Materialia (Oxf) 20 (2021) 101225.

[24] F. Körmann, T. Kostiuchenko, A. Shapeev, J. Neugebauer, B2 ordering in body-centered-cubic AlNbTiV refractory high-entropy alloys, Phys. Rev. Mater. 5 (2021) 053803, https://doi.org/10.1103/PhysRevMaterials.5.053803.

[25] E. Zhang, Y. Tang, M. Wen, A. Obaied, I. Roslyakova, L. Zhang, On phase stability of Mo-Nb-Ta-W refractory high entropy alloys, Int. J. Refract. Met. Hard Mater. 103 (2022) 105780.

[26] E.A. Lass, On the thermodynamics and phase transformation pathways in BCC-B2 refractory compositionally complex superalloys, Metall. Mater. Trans. A 53 (2022) 4481–4498, https://doi.org/10.1007/s11661-022-06844-6.

[27] S. Laube, S. Schellert, A. Srinivasan Tirunilai, D. Schliephake, B. Gorr, H.-J. Christ, A. Kauffmann, M. Heilmaier, Microstructure tailoring of Al-containing compositionally complex alloys by controlling the sequence of precipitation and ordering, Acta Mater. 218 (2021) 117217, https://doi.org/10.1016/j.actamat.2021.117217.

[28] S. Laube, A. Kauffmann, S. Schellert, S. Seils, A.S. Tirunilai, C. Greiner, Y.M. Eggeler, B. Gorr, H.-J. Christ, M. Heilmaier, Formation and thermal stability of two-phase microstructures in Al-containing refractory compositionally complex alloys, Sci. Technol. Adv. Mater. 23 (2022) 692–706, https://doi.org/10.1080/14686996.2022.2132118.

[29] C. Gadelmeier, Y. Yang, U. Glatzel, E.P. George, Creep strength of refractory high-entropy alloy TiZrHfNbTa and comparison with Ni-base superalloy CMSX-4, Cell Rep. Phys. Sci. 3 (2022) 100991, https://doi.org/10.1016/j.xcrp.2022.100991.

[30] C.-J. Liu, C. Gadelmeier, S.-L. Lu, J.-W. Yeh, H.-W. Yen, S. Gorsse, U. Glatzel, A.-C. Yeh, Tensile creep behavior of HfNbTaTiZr refractory high entropy alloy at elevated temperatures, Acta Mater. 237 (2022) 118188, https://doi.org/10.1016/j.actamat.2022.118188.

[31] A. Epishin, B. Fedelich, G. Nolze, S. Schriever, T. Feldmann, M.F. Ijaz, B. Viguier, D. Poquillon, Y. Le Bouar, A. Ruffini, A. Finel, Creep of single crystals of nickel-based superalloys at ultra-high homologous temperature, Metall. Mater. Trans. A 49 (2018) 3973–3987, https://doi.org/10.1007/s11661-018-4729-6.

[32] F.R.N. Nabarro, Rafting in superalloys, Metall. Mater. Trans. A 27 (1996) 513–530, https://doi.org/10.1007/BF02648942.

[33] W. Xia, X. Zhao, L. Yue, Z. Zhang, Microstructural evolution and creep mechanisms in Ni-based single crystal superalloys: a review, J. Alloys. Compd. 819 (2020) 152954, https://doi.org/10.1016/j.jallcom.2019.152954.

[34] H. Mughrabi, The importance of sign and magnitude of γ/γ′ lattice misfit in superalloys—With special reference to the new γ′-hardened cobalt-base superalloys, Acta Mater. 81 (2014) 21–29, https://doi.org/10.1016/j.actamat.2014.08.005.

[35] J.K. Tien, R.P. Gamble, Effects of stress coarsening on coherent particle strengthening, Metall. Trans. 3 (1972) 2157–2162, https://doi.org/10.1007/BF02643227.

[36] A. Bauer, S. Neumeier, F. Pyczak, M. Göken, Creep strength and microstructure of polycrystalline γ'–strengthened cobalt-base superalloys, Superalloys 12 (2012) 695–703.

[37] D. Schliephake, A.E. Medvedev, M.K. Imran, S. Obert, D. Fabijanic, M. Heilmaier, A. Molotnikov, X. Wu, Precipitation behaviour and mechanical properties of a novel Al0.5MoTaTi complex concentrated alloy, Scr. Mater. 173 (2019) 16–20, https://doi.org/10.1016/j.scriptamat.2019.07.033.

[38] N. Yurchenko, E. Panina, Ł. Rogal, L. Shekhawat, S. Zherebtsov, N. Stepanov, Unique precipitations in a novel refractory Nb-Mo-Ti-Co high-entropy superalloy, Mater. Res. Lett. 10 (2022) 78–87, https://doi.org/10.1080/21663831.2021.2022033.

[39] C.H. Belcher, D. Kamp, S. To, Y. Lu, D. Chassaing, T. Boll, B.E. MacDonald, E.M.Y. Lee, D. Apelian, E.J. Lavernia, The origin and control of interstitial impurities in refractory complex concentrated alloys, (2024). https://doi.org/10.2139/ssrn.4865723.

[40] R.W. Balluffi, L.L. Seigle, Growth of voids in metals during diffusion and creep, Acta Metall. 5 (1957) 449–454, https://doi.org/10.1016/0001-6160(57)90063-9.

[41] W. Blum, P. Eisenlohr, F. Breutinger, Understanding creep—A review, Metall. Mater. Trans. A 33 (2002) 291–303, https://doi.org/10.1007/s11661-002-0090-9.

[42] H. Mughrabi, Revisiting "steady-State" monotonic and cyclic deformation: emphasizing the quasi-stationary State of deformation, Metall. Mater. Trans. A 51 (2020) 1441–1456, https://doi.org/10.1007/s11661-019-05618-x.

[43] A.K. Mukherjee, J.E. Bird, J.E. Dorn, Experimental correlations for high-temperature creep, (1968). https://escholarship.org/content/qt31p4z5v2/qt31p4z5v2.pdf (accessed July 23, 2024).

[44] Self-diffusion in pure metals - ScienceDirect, (n.d.). https://www.sciencedirect.com/science/article/pii/0022311578902349 (accessed July 18, 2024).

[45] H. Nakajima, K. Nonaka, W. Sprengel, M. Koiwa, Self-diffusion and interdiffusion in intermetallic compounds, Mater. Sci. Eng. A 239–240 (1997) 819–827, https://doi.org/10.1016/S0921-5093(97)00672-2.

[46] F.R.N. Nabarro, Grain size, stress, and creep in polycrystalline solids, Phys. Solid State 42 (2000) 1456–1459, https://doi.org/10.1134/1.1307052.

[47] W. Österle, D. Bettge, B. Fedelich, H. Klingelhöffer, Modelling the orientation and direction dependence of the critical resolved shear stress of nickel-base superalloy

single crystals, Acta Mater. 48 (2000) 689–700, https://doi.org/10.1016/S1359-6454(99)00404-8.

[48] M. Heilmaier, M. Krüger, H. Saage, J. Rösler, D. Mukherji, U. Glatzel, R. Völkl, R. Hüttner, G. Eggeler, Ch. Somsen, T. Depka, H.-J. Christ, B. Gorr, S. Burk, Metallic materials for structural applications beyond nickel-based superalloys, JOM 61 (2009) 61–67, https://doi.org/10.1007/s11837-009-0106-7.

[49] D.K. Matlock, W.D. Nix, The effect of sample size on the steady state creep characteristics of Ni-6 pct W, Metall. Trans. 5 (1974) 1401–1412, https://doi.org/10.1007/BF02646626.

[50] H. Chen, A. Kauffmann, M. Heilmaier, Unpublished results, (2019).

[51] A. Bauer, S. Neumeier, F. Pyczak, R.F. Singer, M. Göken, Creep properties of different γ′-strengthened Co-base superalloys, Mater. Sci. Eng. A 550 (2012) 333–341, https://doi.org/10.1016/j.msea.2012.04.083.

[52] F. Stein, M. Palm, Re-determination of transition temperatures in the Fe–Al system by differential thermal analysis, Int. J. Mater. Res. 98 (2007) 580–588, https://doi.org/10.3139/146.101512.

[53] G.W.H. Höhne, H.K. Cammenga, W. Eysel, E. Gmelin, W. Hemminger, The temperature calibration of scanning calorimeters, Thermochim. Acta 160 (1990) 1–12, https://doi.org/10.1016/0040-6031(90)80235-Q.

[54] E. Gmelin, St.M. Sarge, Calibration of differential scanning calorimeters, 67 (1995) 1789–1800. https://doi.org/10.1351/pac199567111789.

[55] G.W.H. Höhne, Remarks on the calibration of differential scanning calorimeters, J. Therm. Anal. 37 (1991) 1987–2000, https://doi.org/10.1007/BF01912232.

[56] S.A. Kube, C. Frey, C. McMullin, B. Neuman, K.M. Mullin, T.M. Pollock, Navigating the BCC-B2 refractory alloy space: stability and thermal processing with Ru-B2

precipitates, Acta Mater. 265 (2024) 119628, https://doi.org/10.1016/j.actamat.2023.119628.

[57] C. Frey, On the stability of coherent HfRu- and ZrRu-B2 precipitates in Nb-based alloys, Scr. Mater. (2025).

[58] C. Frey, B. Neuman, A. Botros, S.A. Kube, Tresa.M. Pollock, Refractory multi-principal element alloys with solution and aged HfRu-B2 precipitates, Scr. Mater. 255 (2025) 116411, https://doi.org/10.1016/j.scriptamat.2024.116411.

[59] A. Bezold, N. Volz, F. Xue, C.H. Zenk, S. Neumeier, M. Göken, On the precipitation-strengthening contribution of the Ta-containing Co3(Al,W)-phase to the creep properties of γ/γ′ cobalt-base superalloys, Metall. Mater. Trans. A 51 (2020) 1567–1574, https://doi.org/10.1007/s11661-020-05626-2.

[60] R. Lagneborg, B. Bergman, The stress/creep rate behaviour of precipitation-hardened alloys, Metal Sci. 10 (1976) 20–28, https://doi.org/10.1179/030634576790431462.

[61] B. Reppich, M. Heilmaier, K. Liebig, G. Schumann, K.-D. Stein, T. Woller, Microstructural modelling of the creep behaviour of particle-strengthened superalloys, Steel Res. 61 (1990) 251–257, https://doi.org/10.1002/srin.199000343.

[62] W. Schneider, J. Hammer, H. Mughrabi, Creep deformation and rupture behaviour of the monocrystalline superalloy CMSX-4 - comparison with the alloy SRR 99, in: S.D. Antolovich, R.W. Stusrud, R.A. MacKay, D.L. Anton, T. Khan, R.D. Kissinger, D.L. Klarstrom (Eds.), The Minerals, Metals & Materials Society, 1992.

[63] F. Müller, B. Gorr, H.-J. Christ, H. Chen, A. Kauffmann, S. Laube, M. Heilmaier, Formation of complex intermetallic phases in novel refractory high-entropy alloys NbMoCrTiAl and TaMoCrTiAl: thermodynamic assessment and experimental validation, J. Alloys. Compd. 842 (2020) 155726.